

High resolution compact vertical inertial sensor for atomic quantum gravimeter hybridizing

A. Amorosi^{1,3}, L. Amez-Droz^{1,2}, M. Teloi^{1,3}, M.H. Lakkis^{1,3}, B. Ding³, J. Watchi³, A. Sider¹, C. Di Fronzo¹, R. Jamshidi¹, P. Lambert², C. Collette^{1,3}

¹ Université de Liège, A&M Dept.,

Allée de la Découverte 9, B52/ Quartier Polytec 1, B-4000, Liège, Belgium

email: anthony.amorosi@uliege.be

² Université Libre de Bruxelles, TIPs Dept. CP 165/67

Av. Franklin Roosevelt 50, B-1000, Bruxelles

³ Université Libre de Bruxelles, BEAMS Dept. CP 165/56

Av. Franklin Roosevelt 50, B-1000, Bruxelles

Abstract

We present a novel design of a high resolution compact interferometric inertial sensor intended to extend the bandwidth of an atomic quantum gravimeter. The mechanics of the sensor features fused silica glass flexure joints, allowing to produce a relatively low natural frequency mechanism of 2.8 Hz in a $10 \times 10 \times 10 \text{ cm}^3$, design. We report its quality factor of 2800 in open-air. The linear translation guide allows the motion of the proof-mass to be monitored using an interferometric readout. The readout is based on a custom Michelson interferometer design, which uses laser beam propagating in phase-quadrature to allow a long-range measurement with a relative resolution of $2 \times 10^{-13} \text{ m}/\sqrt{\text{Hz}}$ at 1 Hz. The sensor is operated in closed-loop so as to increase the dynamic bandwidth of the sensor and improve the linearity of the readout. The actuator used for closing the loop is an homemade double-magnet voice-coil, designed to reduce the Eddy-current damping induced by the magnet. This sensor is designed to be compatible with an UHV environment.

1 Introduction

Atomic quantum gravimeters (AQG) are ultra-stable absolute gravity sensors which performance is mainly limited by seismic motion [1, 2, 3]. In addition to this parasitic vibration, atomic interferometers suffer from dead times and a small bandwidth due to their discrete functioning. Different solutions have been proposed to address these issues, consisting mostly of (i) combinations of active/passive vibration isolation of the gravimeter sensor head [4, 5], (ii) real-time vibration compensation on the sensor output [6, 7] or (iii) sensor hybridization [8, 9]. The merging of a gravimeter with a classical accelerometer further allows to compensate dead-times and reduce ground vibrations, hence improving their resolution. Since all these methods uses seismic sensor as a base line, there performance is inherently limited to the resolution of the accelerometer: higher performance accelerometer leads to better vibration compensation.

This paper presents a novel design of an interferometric inertial sensor intended to be used as an accelerometer in vibration compensation techniques of quantum gravimeters. Inertial sensors based on an interferometric readout currently provides performances better than conventional electromagnetic readout seismometers. Sub-picometer resolutions have been achieved using Michelson interferometric readings of the proof-mass motion of inertial sensors [10, 11, 12, 13]. The sensors (VINS and HINS) designed by B. Ding [14] improving the concept of the STS-1 sensor [15]. The VINS has a resolution of $2 \times 10^{-13} \text{ m}/\sqrt{\text{Hz}}$ at 1 Hz and has a principal resonance frequency at 260 mHz. Although this sensor has no match in terms of performance and was used to improve active isolation control strategies [16], it is too large to allow its integration with the

AQG. It must fit in a $10 \times 10 \times 10 \text{ cm}^3$ box. Also, for further use of this sensor in other research projects, we have chosen to design it for operation under high-vacuum. So, a compact and vacuum-compatible inertial sensor that matches the performance of the VINS is then under study. It must operate from 10 mHz to 100 Hz. As it is known that the use of corner cubes adds a parasitic polarization effect, the new sensor features a flat mirror mounted on a fused silica translation flexure guiding. The joint linking the inertial mass to the frame is optimized to maximize the spurious resonances of the mechanism.

Fused silica glass has one of the largest elastic range ($\sigma_{max}/E \approx 0.02$ with σ_{max} , its bending elastic limit and E , its Young's modulus) which makes it an exceptional candidate for compliant mechanism design (the typical σ_{max}/E of Steel and TiAl6V4 are respectively 0.004 and 0.007). For low-frequency inertial sensors ($< 1 \text{ Hz}$), the resolution is usually limited by the thermal noise [17]. The part of the thermal noise which depends on the material comes from the internal damping in the flexure joints. It is quantified as the mechanical loss factor (down to 10^{-5} for fused silica). The precision sensors need also the lowest expansion coefficient ($5.2 \times 10^{-5} \text{ K}^{-1}$ for fused silica). The parts are manufactured by femtosecond laser-assisted etching [18].

In this paper, the sensor mechanics is presented in Section 2. Then, Section 3 is dedicated to the interferometric readout architecture. Next, expanding the sensor's operating range using a custom voice-coil actuator is explained in Section 4. Finally, the performance of the sensor is presented according to its estimated noise budget in Section 5. The modal analysis of the sensor is detailed in the Appendix.

2 Mechanical design

Since the seismic motion is measured using a moving flat mirror, a translation guiding is required to guarantee the reflection of the laser beam in the same axis in the interferometer. Figure 1 shows the mechanics of the proposed inertial sensor. It is inspired by a linear encoder-based inertial sensor designed by Hellegouarch *et al.* [19]. The mirror is placed at the output stage of a parallel four-bar linkage (the rigid part between (2) and (4)). The mass is linked to the fixed frame by only one hinge joint to maximize the spurious resonance frequencies. To maximize the resolution of the sensor, the length of the bar between (1) and (2) shall be maximized. To limit the principal resonance frequency, the radius of gyration shall be maximized. Flexure hinges (2-4) are circular notch hinges. Those joints are only used as guidance for the mirror. Therefore, they do not need to support a significant mass. So, the flexure hinge types are chosen according to their manufacturability and their centre of rotation drift. Henein describes the usual flexures in [20]. Introducing a 3D glass monolithic micro-flexure, Tielen and Bellouard compared their novel flexure hinge with the other usual flexure hinge types [21]. It was shown that the circular notch has the lowest centre of rotation drift, it is even negligible. So, the circular notch hinge is the best choice to limit the non-linearities. Their geometry is chosen according to the manufacturing limitations to limit their stiffness. Concerning the flexure hinge (1), there are two aspects to consider. In the linear encoder-based inertial sensor, the suspension mechanism for the inertial mass consists of applying a prestress in the flexure hinge (1). Since we will primarily use fused silica for the flexures, applying a prestress is difficult or even not possible. As it has been widely used for low-frequency inertial sensors, we chose to use a leaf-spring for the inertial mass suspension. Indeed, E. Whielandt explains that leaf-spring astatic suspensions were invented for that purpose [15]. It combines a small overall size with a long free period. Finally, the flexure hinge (1) type of our current design is a two-part cantilever beam. This flexure is easy to manufacture, can withstand large deflection and can be very thin. This allows to design them wider in order to stiffen the mechanism in the transverse motion direction of the DoF. By studying the mode shape of the 1st spurious resonance on a simplistic design of the mechanics (figure 1d), a kinematic model has been obtained (figure 1e). From this model, to maximize this spurious resonance frequency, it has been shown that the length of the parallel leaf-springs shall be minimized and the distance between them maximized.

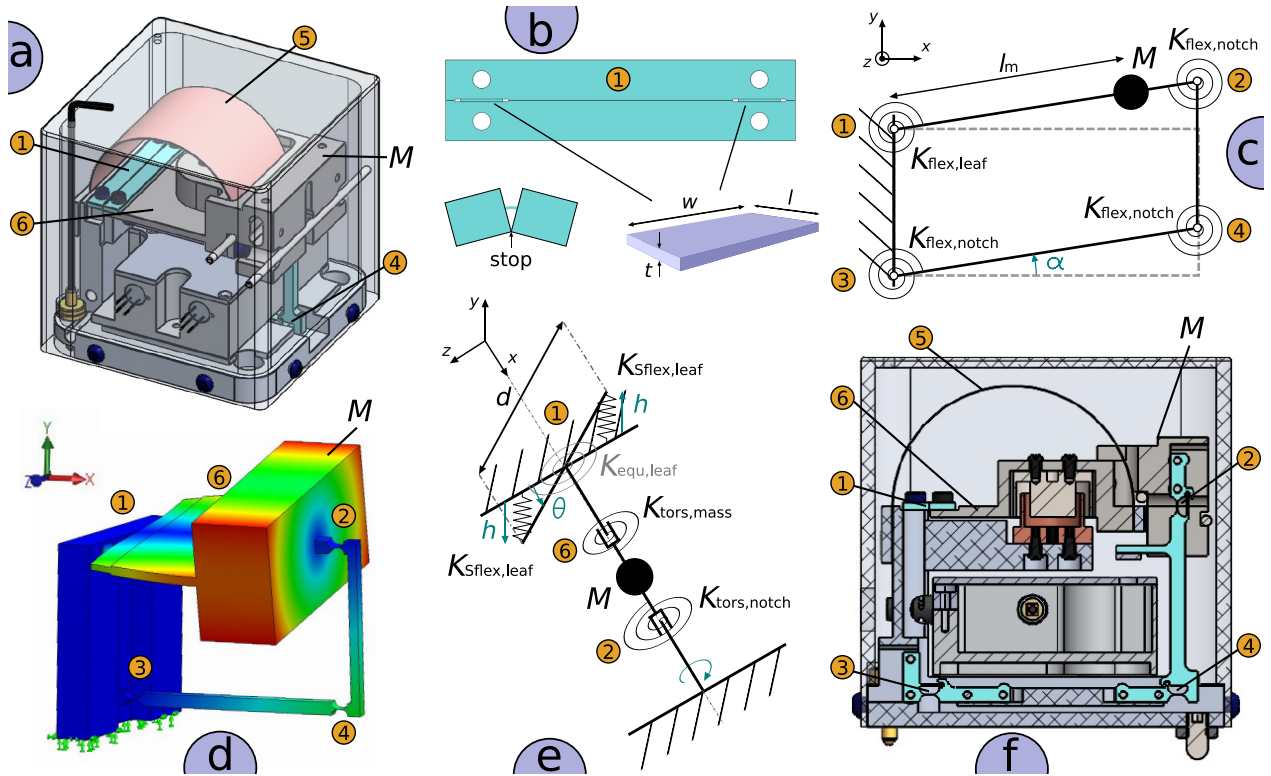


Figure 1: The flexure joints are labelled with numeration. (a) Trimetric view of the sensor construction. (f) Fused silica joints are highlighted in cyan blue. It is composed of a leaf-spring hinge (1) linking the inertial mass M to the frame and 3 circular notch hinges (1-3) transferring the inertial mass motion to the mirror in translation. The mirror is located between (2) and (3). (c) $K_{\text{flex,leaf}}$ and $K_{\text{flex,notch}}$ are the bending stiffnesses of the hinge joints of the translational guiding. α is the rotation angle of the inertial mass M with l_m its radius of gyration. (b) The leaf-spring hinge joint (1) is composed of 2 parallel leaf-springs of width w , length l and thickness t . The motion stops are included in its design. The geometry of these leaf-springs is defined as it maximizes the 1st spurious resonance of the inertial mass. (d) The 1st spurious mode shape is studied using a simplistic design of the mechanics. (e) The pseudo-rigid model of this mode is extracted. $K_{\text{Sflex,leaf}}$ is the double bending stiffness of the leaf-spring, $K_{\text{tors,mass}}$ is the torsional stiffness of the thin part of the inertial mass (6) and $K_{\text{tors,notch}}$ is the torsional stiffness of the circular notch (2). θ is the torsional angle of the inertial mass, h is the deflection of the leaf-springs and d is the distance between their centre. The circular notch hinge (2) has been tilted by 90° (from (d) to (f)) to increase the transverse stiffness of the mirror guiding. The inertial mass is suspended horizontally by a Beryllium Copper bent leaf-spring (5).

The fused silica parts are manufactured by femtosecond laser-assisted etching. Bellouard *et al.* [18] presented that such a method can be used to obtain high-aspect-ratio microfluidic microstructures. This aspect ratio (100:1 with Thorlabs 10x laser lens and using KOH as the etchant) allows us to manufacture monolithic flexible joints even in thick substrates (2 mm and 5 mm). The mirror guiding flexible structures and the leaf-spring hinge joint are obtained respectively from a 5 and a 2 mm fused silica substrate (figure 2a and 2c). The assembly of the inertial mass and its hinge joint is performed using a 6D compliant mounting platform to limit the stress in the flexure hinge (figure 2b). Figure 2d shows the μVINS mechanics fully mounted. To interface this sensor, a plastic part including a Beryllium Copper sheet is mounted on the output stage of the translation guiding. A ringdown experiment is performed using an Eddy-current sensor in an open-air environment. The quality factor of the sensor is obtained (2800) as well as its resonance frequency (2.8 Hz).

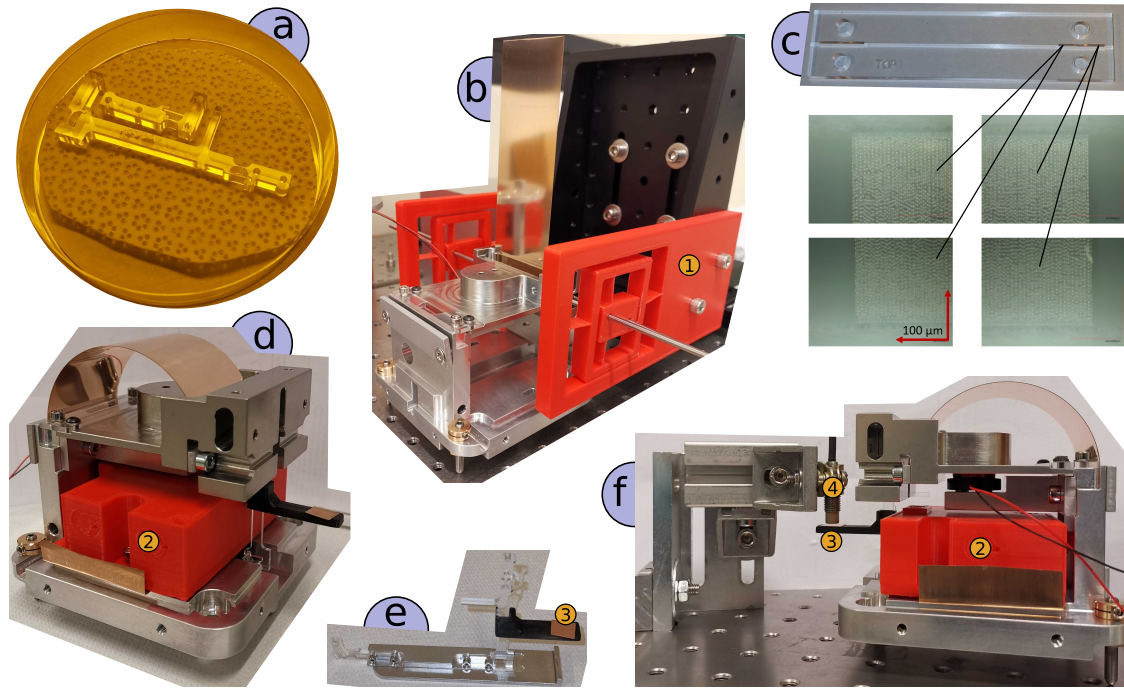


Figure 2: (d) The inertial sensor is mounted with a red dummy interferometric readout box (2). The fused silica flexure joints (a) and (c) are obtained by femtosecond laser-assisted etching. (c) The laser pattern that limits the surface quality of the leaf-springs is visible in the enlarged views (surface roughness $R_a \approx 1 \mu\text{m}$). (b) A 6D compliant custom mounting platform (1) is used to assemble the inertial mass M to the frame with its fused silica leaf-spring hinge joint (c). (e) The mirror guiding is pre-assembled and slid below the inertial mass with the interferometric readout box (2). (f) The first ringdown test is performed using an Eddy-current sensor (4). A plastic mount is attached to the mirror guiding including a Beryllium Copper sheet (3) to interface the Eddy-current sensor.

3 Interferometric readout

Optical readouts based on quadrature, long-range, Michelson interferometry currently allow to reach some of the highest state-of-the-art sensitivity, and are therefore very well suited for measuring very small motions [22, 23, 24, 12, 25]. These readouts have demonstrated sub-picometre resolution when used as sensing elements in inertial devices [16, 26, 11]. The optical scheme of the interferometer used in this sensor is shown in figure 3. The working principle is similar to that of a classical Michelson interferometer: the motion of the proof-mass is read from the interference of two laser beams, after recombination in the arms of the interferometer, where one beam is pointed to a fixed reference mirror and the other beam is pointed to the test-mass. However, the optical scheme features additional polarising elements and photodiodes, allowing the measuring range to be extended over multiple wavelengths, whereas the range of standard Michelson interferometers is limited to motion up to a quarter of the laser wavelength only [22]. Another main advantage of this optical scheme is that the use of three photodiodes allows to subtract the laser intensity noise (RIN) from the readout of the interferometer. The working principle and demodulation technique are extensively discussed in [22, 14, 27].

The electrical and optical components of the interferometer have been specifically chosen for its high resolution and its low-noise performance. The laser source is a Koheras Adjustik X15 Distributed Feedback (DFB) fiber laser. It outputs a single-frequency, 1550 nm wavelength, laser beam with a sub- $\mu\text{rad}/\text{m}/\sqrt{\text{Hz}}$ phase noise at frequencies higher than 10 Hz. The laser beam is fed to the interferometer via a FC/APC polarisation maintaining optical fiber with an optical power of 4mW. The photodiodes are Thorlabs FGA21 InGaAs photodiodes, characterised by a responsivity $R = 1.04 \text{ A/W}$ and a Noise Equivalent Power (NEP) of $6 \times 10^{-14} \text{ W}/\sqrt{\text{Hz}}$ at the laser wavelength. They are operated in a photoconductive mode, under a bias

voltage of 2.5 V, leading to a typical dark current of 50 nA. The photocurrent is processed by a custom transimpedance amplifier with a feedback resistor of 10 k Ω . The electrical components of the circuit, especially resistors, have been chosen to have Noise Indexes lower than -30 dB so as to reduce the Flicker, $1/f$ noise. More on noise estimation and budgeting is discussed in Section 5. The output voltage is then recorded by a 16-bit, real-time, Microlab Box Analog-to-digital converter.

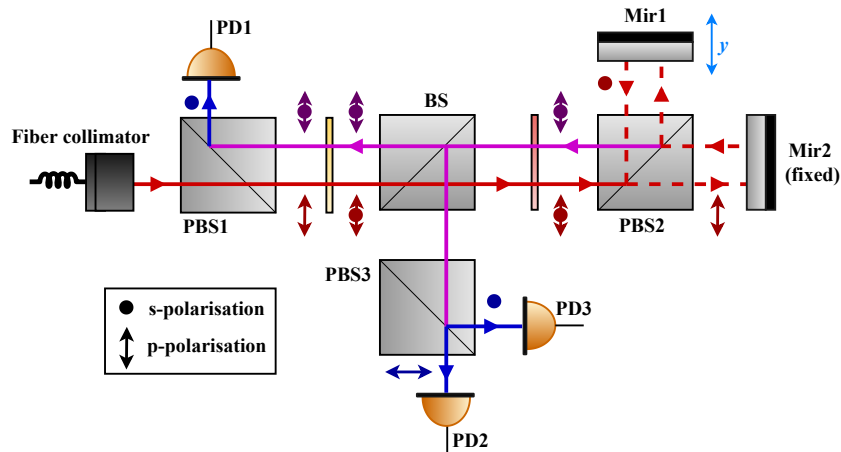


Figure 3: Quadrature interferometer optical scheme. The optical path to the retro-reflecting mirrors Mir1 and Mir2 is shown in red, while the reflected path is shown in purple. The light intensities detected at the photodiodes are shown in blue. The polarisation state of the laser beam is indicated using arrows (p-polarisation) or a dot (s-polarisation) [16].

4 Voice-coil actuator

The sensor is operated in closed loop to take advantage of the Force Balance Principle [28, 29]. Feeding back the motion of the proof-mass read by the interferometer to a force actuator through an appropriate PID controller allows to electronically freeze the motion of the mass. Conceptually, the sensor output is no longer the proof-mass motion but rather the force required to keep it still. This technique improves the linearity of the sensor and extends its dynamic range and bandwidth. It is worth mentioning that this however has no impact nor on the noise level of the sensor nor on the signal-to-noise ratio. Voice-coil actuators are very popular for this application. Due to their contactless actuation, they can be mounted at any location on the sensor with minimal impact on the dynamic of the system. However, the permanent magnet of the voice-coil has experimentally been reported to generate Eddy currents in both the moving, conductive, parts in the vicinity of the actuator and in the wiring of the coil itself [30]. In turn, these Eddy currents dissipate the kinetic energy of the system into heat, adding damping to the system. Since the generation of these Eddy currents is directly proportional to velocity, this source of damping directly translates into noise according to the Fluctuation-Dissipation theorem [17]. A carefully designed magnet allows to greatly reduce Eddy-current generation and therefore spurious damping [30, 31, 32, 33]. The novel magnet design consists of a pair of two like-pole facing magnets. This configuration leads to a resulting magnetic field whose intensity decays as R^{-4} , R being the radial distance from the magnet, whereas a single traditional magnet shows a R^{-3} decay.

A custom magnet has been designed to balance the motion of the mass for usual seismic activity, while still fitting in the mechanics of the sensor with an acceptable clearance. The magnet design has been optimised to generate the required Lorentz force under minimal excitation current. The optimisation process is based on the fundamental equations of electromagnetism and the Biot-Savart law, and is extensively described in [30]. Figure 4 shows a schematic drawing of the design of the custom double-magnet. N45 Neodymium disc magnets are used for their large magnetic strength. The magnets are 12 mm in diameter and 3 mm thick to fit the mechanics with an acceptable clearance to allow rotation motion of the pendulum and an easy alignment.

A 5 mm inter-magnet distance has been optimised to allow a good far-field cancellation of the magnetic flux lines, but still allowing an acceptable force per unit current to be generated by the coil.

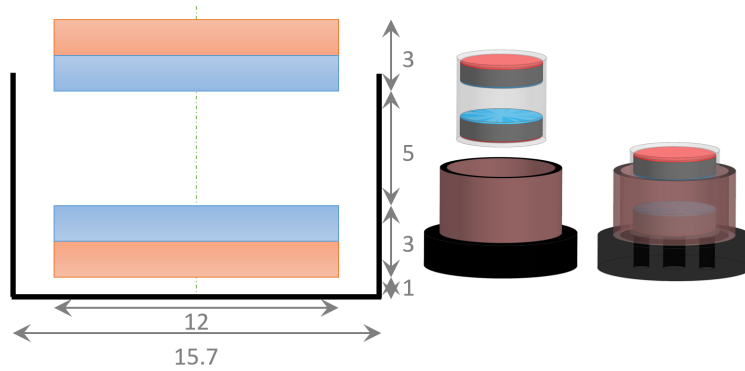


Figure 4: Schematic drawing of the double magnet voice-coil (left) and CAD view (right). The Neodymium magnets are shown as the blue/orange blocks, the coil is drawn in black and characteristic dimensions are shown in grey. The double magnet assembly is embedded in a casing made of a non-magnetic material.

The force constant of the magnet actuator has been modelled and is depicted in Figure 5. It shows that the voice-coil has a force constant of 0.59 N/A when the magnet is in optimal configuration, i.e. when it is off-centered by about 2.5 mm from the coil center. Assuming a rms value for the ground motion of typically a few micrometres, it can be computed from the pendulum inertia and location of the force actuator that an average of 5 mN would be required to balance the pendulum motion. This leads to a reasonable average actuation current of 8.5 mA.

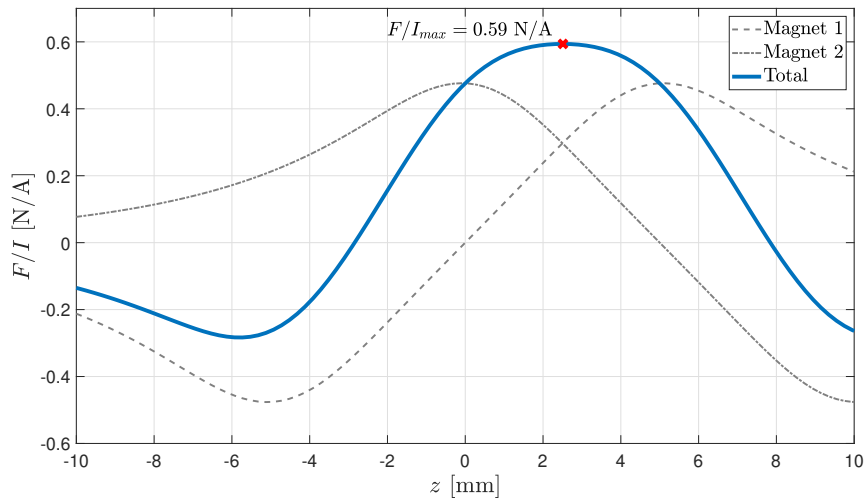


Figure 5: Force per unit current of the custom voice-coil. z represents the distance of the magnet assembly to the coil center. The Lorentz forces applied on each individual magnets are shown as grey lines, and the resulting force is shown in blue. The voice-coil has a maximum force constant of 0.6 N/A in the optimal position.

The voice-coil has been produced and experimentally characterised. The experimental setup is shown in figure 6. The force constant has been measured by mounting the voice-coil on a scale, and measuring the pulling/pushing force of the actuator when injecting constant current to the coil. The weight reading of the scale can be up-converted to a force by multiplying the mass reading by the gravitational acceleration. The scale allows a reading accuracy of 0.01 g. The voice-coil demonstrated a force constant of 0.6465 N/A, and a good linearity even under input currents larger than 50 mA.

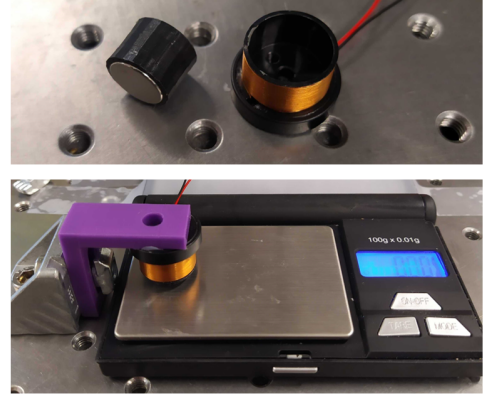
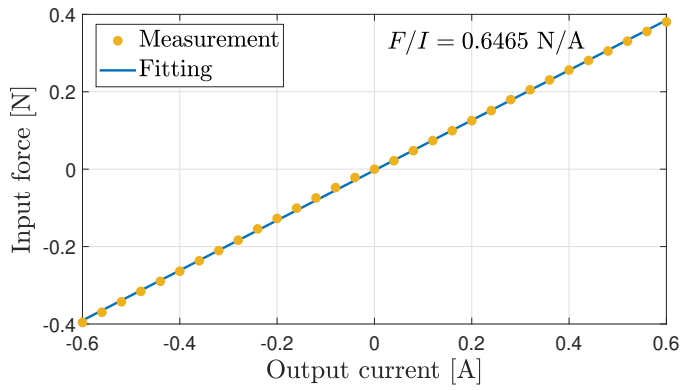


Figure 6: Force output of the custom voice-coil actuator fed with DC current (left) and experimental setup (right). The voice-coil was mounted on a scale and fed with DC current. The weight reading on the scale can be upconverted to a force reading measurement. The force constant of 0.6465 N/A have been measured.

5 Estimated performance

The sensor resolution represents the smallest quantity that can be measured, i.e. the smallest quantity that can be coherently distinguished from noise. It can therefore be assessed from the different noise sources affecting the output signal of the sensor. Because of the random nature of the noise sources, they are better evaluated in the frequency domain, using the power spectral density formalism. If every source of noise can be assumed to be uncoherent, which most often is the case in practice, the power spectral density of the inertial sensor is the sum of the power spectral densities of each noise source.

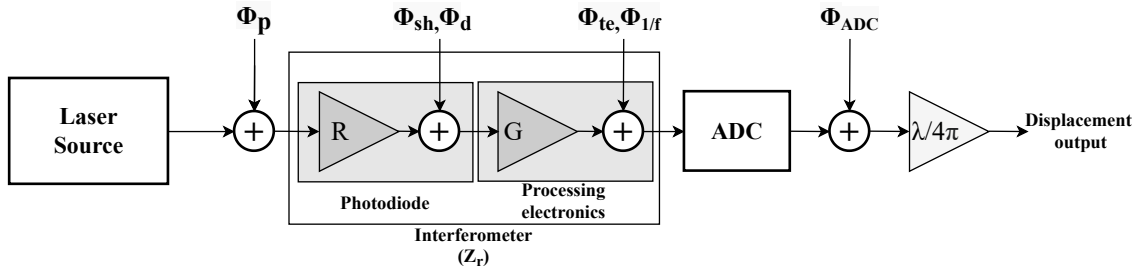


Figure 7: Global noise modelling of the interferometer. Φ_p is the laser phase noise, Φ_{sh} and Φ_d the photodiode shot and dark current noise, Φ_{te} and $\Phi_{1/f}$ the thermoelectrical and $1/f$ noise in the processing unit and Φ_{ADC} the DAQ noise. The arrow shows the direction the information 'flows'. The laser power is converted at the photodiode level to a current reading via the photodiode responsivity R (A/W). This current is converted to an analog voltage in the processing unit with a conversion factor G (V/A). Z_r represents to total load impedance of the detection circuit (Ω). The ADC records the analog signal and converts it to a digital voltage that is finally converted to displacement as discussed in Section 3 [22].

In inertial sensors, noise sources can be categorised in mechanical noise sources and readout noise sources [34, 29]. The mechanical noise refers to a mechanical motion of the proof-mass under thermal effects, while the readout noise refers to the voltage noise arising from the interferometric readout. The thermal noise can be further decomposed into two major contributions [35, 30]: Brownian thermal noise (i) and (ii) structural thermal noise. Brownian thermal noise is caused by the thermal agitation of gas molecules, which collide and exchange part of their momentum with the test-mass. The definition can be extended to any velocity-dependent damping phenomenon, such as Eddy-current damping. On the other hand, structural thermal noise corresponds to intrinsic losses within the material. A strong influence of the pressure on the Brownian thermal noise have been experimentally observed and modelled [36]. Brownian thermal noise is usually

the limiting factor when operating at ambient pressure. However, at pressure level below typically 10^{-3} mbar, thermal noise becomes structural damping limited. This latter being essentially a material properties. For minimizing thermal noise, the sensor therefore operates in a High-Vacuum environment below 10^{-3} mbar, and flexible elements are made of fused-silica, for which structural Q-factors larger than 10^6 have been reported [37]. This motivates the use of the sensor in a high-vacuum environment and the use of the fused-silica joints. Both sources of thermal noise can be modelled from the fluctuation-dissipation theorem [17].

On the other hand, the resolution of the interferometer can be further decomposed into its own sources of internal noise. They are essentially: (iii) optical noises and (iv) electrical noises in the processing units and Digital-to-Analog converter. The optical noise further includes the photodiodes dark-current noise and shot noise, resulting respectively from a constant current flowing through the p-n junction of the photodiode when a bias voltage is applied, and random jumps of charge carriers across the p-n junction [38]. To this also adds the laser phase and frequency noise. However, since the laser intensity noise is safely discarded in the demodulating process explained in Section 3, only the frequency noise is relevant. The electronic noise is composed of thermoelectrical noise in the resistive elements of the circuit [39], $1/f$ or Flicker, noise in semiconductor devices [40] and Analog-to-Digital noise in the data acquisition system. The modelling of these individual sources of noise is discussed in [22, 34]. These sources of noise add up and translate into the displacement output of the readout system as shown in figure 7. When using an actuator for applying the force balance principle, an additional source (v) corresponding to actuator noise should be included. This noise depends on the electronic used to drive the voice-coil actuator, which is currently under development and requires further investigations. This noise is therefore not included in the analysis. Preliminary results however indicate that it is unlikely to be a limitation.

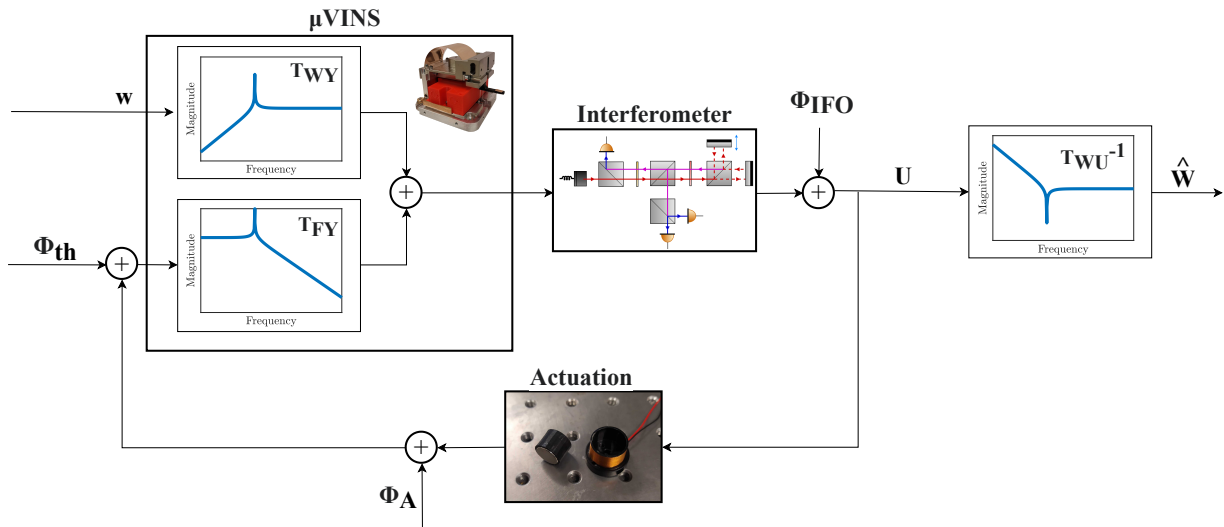


Figure 8: Global noise modelling of the μ VINS sensor. Φ_{IFO} the readout noise, regrouping both the electrical and optical noises as shown in Figure 7; Φ_{th} the thermal noise regrouping both the Brownian $\Phi_{\text{th,B}}$ and structural noises $\Phi_{\text{th,s}}$; and Φ_{A} the actuation noise. T_{WY} , T_{FY} and T_{WU}^{-1} are the transfer function relating ground motion W , and external force F to the proof-mass relative motion Y and the sensor output U .

Finally, all of the above motion sources of noise can be summed together to obtain the global noise floor of the inertial sensor. They have to be scaled by the proper transfer functions of the sensor mechanics in order to convert these noises to their equivalent proof-mass relative motion as shown in figure 8. The reading of the sensor is further scaled by the inverse of the sensor sensitivity transfer function to obtain the minimal, absolute, ground motion that can be sensed.

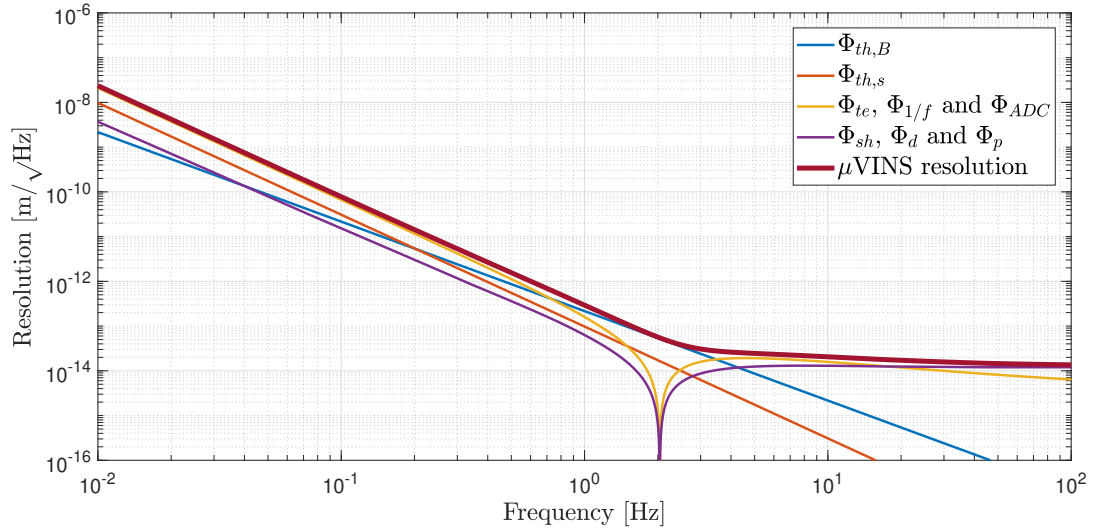


Figure 9: μ VINS noise budgeting. The global noise floor is shown as the red line. $\Phi_{th,B}$ is the Brownian thermal noise, $\Phi_{th,s}$ is the structural thermal noise. Φ_{te} , $\Phi_{1/f}$ and Φ_{ADC} are the thermoelectrical, Flicker and ADC noise, they are shown together as they all represent the electrical sources of noises in the sensor. Φ_{sh} , Φ_d and Φ_p are the photodiode shot noise, dark-current noise and laser phase noise, they are shown together as they all represent optical sources of noises in the sensor. μ VINS is estimated to be characterised by a sensitivity of $1 \times 10^{-10} \text{ m}/\sqrt{\text{Hz}}$, $4 \times 10^{-12} \text{ m}/\sqrt{\text{Hz}}$ and $2 \times 10^{-14} \text{ m}/\sqrt{\text{Hz}}$ at 0.1 Hz, 1 Hz and 100 Hz, respectively.

The estimated resolution of the μ VINS sensor is shown in figure 9. It reaches a sensitivity of $1 \times 10^{-10} \text{ m}/\sqrt{\text{Hz}}$, $4 \times 10^{-12} \text{ m}/\sqrt{\text{Hz}}$ and $2 \times 10^{-14} \text{ m}/\sqrt{\text{Hz}}$ at 0.1 Hz, 1 Hz and 100 Hz, respectively. The sensor is estimated to be electrical noise-limited at low frequencies, mostly related to the $1/f$ Flicker noise in semiconductive components and the ADC noise. At high frequencies above 100 Hz, the sensor resolution hits the dark-current noise of the photodiodes.

6 Conclusion

This paper presents the design concept of a vertical compact low-frequency interferometric inertial sensor μ VINS. The sensor is intended to be an upgraded version of the Vertical INterferometric Sensor (VINS) [14]. Improvements namely consists of (i) a linearly guided motion of a mirror linked to the rotational motion of the proof-mass (ii) a decreased internal thermal noise, (iii) a high-vacuum compatibility of the system, (iv) a lower noise interferometric readout, (v) a closed-loop operation of the sensor and (iv) a size reduction of the sensor down to $10 \times 10 \times 10 \text{ cm}^3$. The linear guide linked to the proof-mass allows to replace the corner cubes of the interferometric readout by flat mirrors, therefore suppressing the nonlinear polarisation noise induced by the corner cubes. The guide is made out of home-made fused-silica joints. Fused-silica is known for having a loss angle better than 10^{-5} [37], greatly reducing the structural thermal noise of the VINS sensor using metallic joints. The full sensor is vacuum compatible and is intended to operate in a high-vacuum environment better than 10^{-3} mbar to significantly reduce Brownian thermal noise. The interferometer resolution is improved using low noise optics and electronics. In order to extend the dynamic bandwidth of the sensor and improve linearity, the sensor is in a feedback loop, following the force-balance principle. The actuator used to apply the feedback force is a voice-coil actuator made of a custom, like-poles facing, double-magnet in order to decrease the Eddy-current induced damping in the metallic part of the material. Experimental testing of the sensor mechanics validate the numerical models. The sensor is characterised with a first natural frequency at 2.8 Hz and has a Q -factor of 2800 in open air. The performance of the sensor when coupled with the interferometric readout is estimated to be $1 \times 10^{-10} \text{ m}/\sqrt{\text{Hz}}$, $4 \times 10^{-12} \text{ m}/\sqrt{\text{Hz}}$ and $2 \times 10^{-14} \text{ m}/\sqrt{\text{Hz}}$ at 0.1 Hz, 1 Hz and 100 Hz, respectively. This represents one order of magnitude of improvement

compared to the VINS sensor, despite the size reduction of the sensor. Furthermore, the resolution of μ VINS shows approximately a 40 dB (ref. $(\text{m/s}^2)^2/\text{Hz}$) improvement in the [0.01 - 100] Hz bandwidth compared to commercial accelerometers used in vibration compensation system in quantum gravimeters, such as the nanometric Titan accelerometer [8, 7]. This is expected to have a significant impact on the vibration rejection in such devices. Further work will report the experimental verification of the estimated performance of the sensor. Also, a conception method to decrease the resonance frequency by adding negative stiffness to the mechanism is currently under investigation.

Acknowledgements

The authors gratefully acknowledge the European Research Council, Consolidator grant SILENT (grant agreement number 866259), and the "Fonds de la Recherche Scientifique", Research project grant INFuSE (grant agreement number FNRS PDR T.0049.20), for funding this research. The authors thank Adam Chafaï of the Micro-Milli Platform, ULB, for supporting the manufacturing of fused silica parts. The authors also acknowledge the LIGO scientific community for reviewing this research. This paper has been assigned the LIGO DCC number P2200207.

References

- [1] Q. Bodart, S. Merlet, N. Malossi, F. P. D. Santos, P. Bouyer, and A. Landragin, "A cold atom pyramidal gravimeter with a single laser beam," *Applied Physics Letters*, vol. 96, no. 13, p. 134101, mar 2010.
- [2] J. L. Gouët, T. E. Mehlstäubler, J. Kim, S. Merlet, A. Clairon, A. Landragin, and F. P. D. Santos, "Limits to the sensitivity of a low noise compact atomic gravimeter," *Applied Physics B*, vol. 92, no. 2, pp. 133–144, jun 2008.
- [3] A. Peters, K. Y. Chung, and S. Chu, "Measurement of gravitational acceleration by dropping atoms," *Nature*, vol. 400, no. 6747, pp. 849–852, aug 1999.
- [4] W. Gong, A. Li, C. Huang, H. Che, C. Feng, and F. Qin, "Effects and Prospects of the Vibration Isolation Methods for an Atomic Interference Gravimeter," *Sensors*, vol. 22, no. 2, p. 583, jan 2022.
- [5] M.-K. Zhou, Z.-K. Hu, X.-C. Duan, B.-L. Sun, L.-L. Chen, Q.-Z. Zhang, and J. Luo, "Performance of a cold-atom gravimeter with an active vibration isolator," *Physical Review A*, vol. 86, no. 4, oct 2012.
- [6] S. Merlet, J. L. Gouët, Q. Bodart, A. Clairon, A. Landragin, F. P. D. Santos, and P. Rouchon, "Operating an atom interferometer beyond its linear range," *Metrologia*, vol. 46, no. 1, pp. 87–94, jan 2009.
- [7] V. Ménoret, P. Vermeulen, N. L. Moigne, S. Bonvalot, P. Bouyer, A. Landragin, and B. Desruelle, "Gravity measurements below 10^{-9} g with a transportable absolute quantum gravimeter," *Scientific Reports*, vol. 8, no. 1, aug 2018.
- [8] J. Lautier, L. Volodimer, T. Hardin, S. Merlet, M. Lours, F. P. D. Santos, and A. Landragin, "Hybridizing matter-wave and classical accelerometers," *Applied Physics Letters*, vol. 105, no. 14, p. 144102, oct 2014.
- [9] P. Cheiney, B. Barrett, S. Templier, O. Jolly, B. Battelier, P. Bouyer, H. Porte, and F. Napolitano, "Demonstration of a robust hybrid classical/quantum accelerometer," in *2019 IEEE International Symposium on Inertial Sensors and Systems (INERTIAL)*. IEEE, apr 2019.
- [10] M. Zumberge, J. Berger, J. Otero, and E. Wielandt, "An optical seismometer without force feedback," *Bulletin of the Seismological Society of America*, vol. 100, no. 2, pp. 598–605, mar 2010.

- [11] S. J. Cooper, C. J. Collins, L. Prokhorov, J. Warner, D. Hoyland, and C. M. Mow-Lowry, “Interferometric sensing of a commercial geophone,” *Classical and Quantum Gravity*, vol. 39, no. 7, p. 075023, mar 2022.
- [12] J. V. van Heijningen, A. Bertolini, and J. F. J. van den Brand, “A novel interferometrically read out inertial sensor for future gravitational wave detectors,” in *2018 IEEE Sensors Applications Symposium (SAS)*. IEEE, mar 2018.
- [13] C. Collette, F. Nassif, J. Amar, C. Depouhon, and S.-P. Gorza, “Prototype of interferometric absolute motion sensor,” *Sensors and Actuators A: Physical*, vol. 224, pp. 72–77, apr 2015.
- [14] B. Ding, “Development of High Resolution Interferometric Inertial Sensors,” Ph.D. dissertation, Université Libre de Bruxelles, 2021.
- [15] E. Wielandt, *Seismometry*. Elsevier, 2002, vol. 81, pp. 283–304.
- [16] B. Ding, G. Zhao, J. Watchi, A. Sider, and C. Collette, “An interferometric inertial sensor for low-frequency seismic isolation,” *Sensors and Actuators A: Physical*, vol. 335, p. 113398, mar 2022.
- [17] P. R. Saulson, “Thermal noise in mechanical experiments,” *Physical Review D*, vol. 42, no. 8, pp. 2437–2445, oct 1990.
- [18] Y. Bellouard, A. Champion, B. Lenssen, M. Matteucci, A. Schaap, M. Beresna, C. Corbari, M. Gecevičius, P. Kazansky, and O. Chappuis, “The femtoprint project,” *Journal of Laser Micro/Nanoengineering*, vol. 7, no. 1, pp. 1–10, 2012.
- [19] S. Hellegouarch, L. Fueyo Roza, K. Artoos, P. Lambert, and C. Collette, “Linear encoder based low frequency inertial sensor,” *International Journal of Optomechatronics*, vol. 10, no. 3-4, pp. 120–129, 2016.
- [20] S. Henein, “Conception des structures articulées à guidages flexibles de haute précision,” EPFL, Report, 2000.
- [21] V. Tielen and Y. Bellouard, “Three-dimensional glass monolithic micro-flexure fabricated by femtosecond laser exposure and chemical etching,” *Micromachines*, vol. 5, no. 3, pp. 697–710, 2014.
- [22] J. Watchi, S. Cooper, B. Ding, C. M. Mow-Lowry, and C. Collette, “Contributed Review: A review of compact interferometers,” *Review of Scientific Instruments*, vol. 89, no. 12, p. 121501, dec 2018.
- [23] J. Watchi, “Active seismic isolation using interferometric inertial sensors,” Ph.D. dissertation, Université Libre de Bruxelles, 2022.
- [24] S. J. Cooper, C. J. Collins, A. C. Green, D. Hoyland, C. C. Speake, A. Freise, and C. M. Mow-Lowry, “A compact, large-range interferometer for precision measurement and inertial sensing,” *Classical and Quantum Gravity*, vol. 35, no. 9, p. 095007, mar 2018.
- [25] V. Greco, G. Molesini, and F. Quercioli, “Accurate polarization interferometer,” *Review of Scientific Instruments*, vol. 66, no. 7, pp. 3729–3734, jul 1995.
- [26] B. Ding, G. Zhao, J. Watchi, and C. Collette, “Huddle test of optical inertial sensors combined with slightly damped mechanics,” 2018.
- [27] J. D. Otero, “Development and Characterization of an Observatory-class, Broadband, Non-Feedback, Leaf-Spring Interferometric Seismometer,” Ph.D. dissertation, University of California, 2009.
- [28] A. Plešinger and J. Buben, “Analysis and optimization of wide-band force-balance seismometer responses,” *Studia Geophysica et Geodaetica*, vol. 28, no. 1, pp. 67–81, mar 1984.

- [29] M. A. Riedesel, J. A. Orcutt, and R. D. Moore, "Limits of sensitivity of inertial seismometers with velocity transducers and electronic amplifiers," *Bulletin of the Seismological Society of America*, vol. 80, no. 6A, pp. 1725–1752, Dec. 1990.
- [30] G. Fortman, "Instruments for seismic isolation," Ph.D. dissertation, Delft University of Technology, 2019.
- [31] A. Mitchell, "Coil drivers with shielding magnets in the 6d inertial isolation system," *LIGO Document T2100132*, 2021.
- [32] A. Mitchell, A. Ubhi, C. Mow-Lowry, and L. Prokhorov, "Coil drivers with shielding magnets in the 6d inertial isolation system," *LVK conference poster*, 2021.
- [33] N. Robertson, "Beamsplitter actuation: Potential use of shielding magnets." *LIGO Document T1500535*, 2019.
- [34] C. Collette, S. Janssens, P. Fernandez-Carmona, K. Artoos, M. Guinchard, C. Hauviller, and A. Preumont, "Review: Inertial Sensors for Low-Frequency Seismic Vibration Measurement," *Bulletin of the Seismological Society of America*, vol. 102, no. 4, pp. 1289–1300, aug 2012.
- [35] B. Boom, "Acceleration sensing at the nano-g level, development and characterisation of low-noise microseismometers for next generation gravitational wave detectors," Ph.D. dissertation, Vrije Universiteit Amsterdam, 2020.
- [36] S. Bianco, M. Cocuzza, S. Ferrero, E. Giuri, G. Piacenza, C. F. Pirri, A. Ricci, L. Scaltrito, D. Bich, A. Merialdo, P. Schina, and R. Correale, "Silicon resonant microcantilevers for absolute pressure measurement," *Journal of Vacuum Science & Technology B: Microelectronics and Nanometer Structures*, vol. 24, no. 4, p. 1803, 2006.
- [37] A. Hines, L. Richardson, H. Wisniewski, and F. Guzman, "Optomechanical Inertial Sensors," 2020.
- [38] P. J. Esrom, "Sensors and signal conditioning, by r. pallas-areny and j.g. webster j. wiley and sons, new york and chichester (uk), 1991 xii 398pp., index (£47.50)." *Robotica*, vol. 10, no. 5, p. 472–472, 1992.
- [39] J. B. Johnson, "Thermal agitation of electricity in conductors," *Phys. Rev.*, vol. 32, pp. 97–109, Jul 1928. [Online]. Available: <https://link.aps.org/doi/10.1103/PhysRev.32.97>
- [40] T. van der Poel, "An exploration of active hard mount vibration isolation for precision equipment," Ph.D. dissertation, 2010.

Appendix

A μ VINS design details

A.1 Resonance frequency of the 1st mode of motion

The resonance frequency is characterized by the stiffness of the link to the ground of the inertial mass and by its inertia. Its stiffness K_{equ} can be obtained as follows (figure 1c):

$$K_{equ} = K_{flex,leaf} + 3K_{flex,notch} + K_{suspension} \quad (1)$$

We chose $K_{flex,leaf} = K_{flex,notch}$ to keep the symmetry of the parallelogram table guidance. We chose to neglect $K_{suspension}$ since a good model to characterize it is not available yet (we are working on it). Then, only the stiffness of the translation guiding is considered. Thus:

$$K_{equ} = 4K_{flex,notch} \quad (2)$$

The circular notch hinge stiffness can be approximated as described in [20]:

$$K_{flex,notch} \simeq \frac{2Ebe^{2.5}}{9\pi\sqrt{r}} \quad (3)$$

with e , its central thickness, b , its width, r , its central radius and E , the Young's modulus of fused silica glass (72 GPa). Lower thickness can be obtained with femtosecond laser assisted etching process, up to 10 μ m. However, it is very fragile. The chosen thickness is a compromise between small thickness and handling easiness. To reduce the width of the rigid bodies, the radius of the notch is reduced to 2 mm at the sides.

The principal resonance frequency is then:

$$f_0 = \frac{1}{2\pi} \sqrt{\frac{K_{equ}}{I_z}} \quad (4)$$

considering $I_z = Ml_1^2$:

$$f_0 = \frac{1}{2\pi} \sqrt{\frac{4K_{flex,notch}}{Ml_1^2}} \quad (5)$$

A.2 Maximization of the operating range

The working range of the inertial sensor is limited by its spurious resonances above the principal resonance frequency. The placement and geometry of the joints can be optimized to stiffen the mechanism except in its principal DoF. Figure 1 shows that the critical joint is the (1). Indeed, that joint links directly the inertial mass to the structure of the sensor.

A.2.1 Method

First, a glass monolithic simple design is defined to simplify the calculations (figure 10b). The structure of the sensor on the left end side of figure 10b is fixed to the ground at its base.

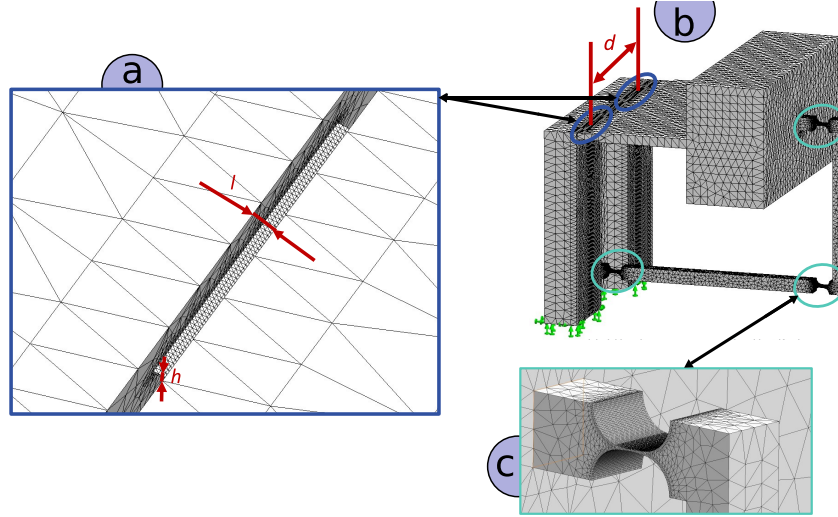


Figure 10: The simplistic design used for the modal analysis (b). The mesh control used for the flexure hinges is 0.1 mm (a and c). The input parameters of the experiment are d , the distance between the centers of the leaf-springs, h , their thickness and l , their length.

To optimize the joint, an experiment plan is defined. A three-factor factorial experiment is defined. The inputs are the thickness of the two leaf-springs, their length and the distance separating each other (figure 10a and 10b). The output of the experiment is the first spurious resonance frequency after the principal resonance frequency. The principal resonance frequency is also computed to verify that the compliance of the mechanism has not been changed.

The width w of the leaf-spring flexure hinge depends on its thickness and its length. It is computed as follows knowing the fixed stiffness of the flexure hinge $K_{flex,leaf} = K_{flex,notch}$:

$$I_z = \frac{w_{tot}h^3}{12} \quad (6)$$

$$K_{flex,leaf} = \frac{EI_z}{l} = \frac{Ew_{tot}h^3}{12l} \quad (7)$$

$$w = \frac{1}{2}w_{tot} = \frac{6lK_{flex,leaf}}{Eh^3} \quad (8)$$

The values are chosen as follows:

- The thickness: from 50 μm which is the lowest possible for manufacturing without significant complications. Then the maximum value is arbitrarily double.
- The length: 0.5 mm is the lowest possible for manual assembly without significant complications (if metal clamped leaf-springs are required). The maximum value is arbitrarily 2 mm.
- The distance between flexure width midpoint: 30 mm is the minimum value where the leaf-springs are merged for the widest case. 50 mm is the maximum value where the leaf-springs external edges are located at the edges of the inertial mass for the widest case.

Table 1: List of experiments

Experiment	thickness h [μm]	length l [mm]	distance d [mm]
000	50	0.5	30
001	50	0.5	50
010	50	2	30
011	50	2	50
100	100	0.5	30
101	100	0.5	50
110	100	2	30
111	100	2	50
Center	75	1	40

The experiments are into two parts. First, a numerical resolution is executed using the simulation toolbox of SolidWorks. Then, from the results of the simulation, an analytical model is identified. Finally, the results are compared between the numerical approach and the analytical approach.

Numerical approach A computer-aided design for each experiment is edited on SolidWorks. Then, a standard mesh is applied to the designs with $r = 2.5$ mm including mesh control with $r = 0.1$ mm on the flexure surfaces (figure 10). Finally, the frequency simulation study is applied.

Analytical approach Regarding the simulation results of the numerical simulation, it appears that the first spurious mode is the torsion mode of the oscillator for every experiments (figure 1d). Figure 1d shows that there is a static point on the top of the rigid body between flexure hinges (2) and (3) after the circular notch next to the inertial mass. A simple analytical model can be identified (figure 1e).

There are three compliant parts on this pseudo-rigid model: the double bending of the leaf-springs in opposition (1), the torsion of the flat part of the inertial mass (6) and the torsion of the circular notch (2). Figure 1e shows that the double bending of the leaf-springs $K_{Sflex,leaf}$ with h deformation can be projected in $K_{equ,leaf}$ with a torsion θ :

$$\frac{1}{2}K_{equ,leaf,approx}\theta^2 = 2\frac{1}{2}K_{Sflex,leaf}h^2 \quad (9)$$

considering $h = \frac{d}{2}\sin(\theta) \approx \frac{d}{2}\theta$:

$$K_{equ,leaf,approx} = \frac{d^2}{2}K_{Sflex,leaf} \quad (10)$$

To consider the double bending stiffness of the leaf-springs in opposition of a height h as a torsion stiffness of an angle θ , an approximation has been made that the deformation of the leaf-spring is constant along with its width. However, it is possible to compute the equivalent torsion stiffness considering an integration of double bent leaf-springs of width dz :

$$K_{equ,leaf} = \frac{2K_{Sflex,leaf}}{w} \int_{\frac{d}{2}-\frac{w}{2}}^{\frac{d}{2}+\frac{w}{2}} z^2 dz \quad (11)$$

with the dimensions in figure 10.

Then, there are two links between the mass M and the "ground" to consider to identify the stiffness in torsion of the inertial mass. There are the first considering the compliance of the flat mass and the leaf-springs in series and the second considering the compliance of the circular notch:

$$K_{equ} = \frac{K_{equ,leaf}K_{tors,mass}}{K_{equ,leaf} + K_{tors,mass}} + K_{tors,notch} \quad (12)$$

Then, the resonance frequency of the torsion mode is obtained as follows:

$$f_{torsion} = \frac{1}{2\pi} \sqrt{\frac{K_{equ}}{I_x}} \quad (13)$$

with I_x the inertia of the inertial mass in its torsion axis x :

$$I_x = \frac{1}{12}(w_1^2 + c_1^2)M_1 + \frac{1}{12}(w_1^2 + c_2^2)M_2 \quad (14)$$

considering the mass dimensions in figure 11.

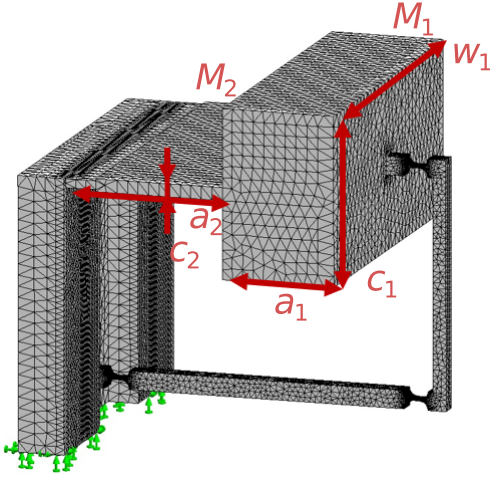


Figure 11: Inertial mass dimensions

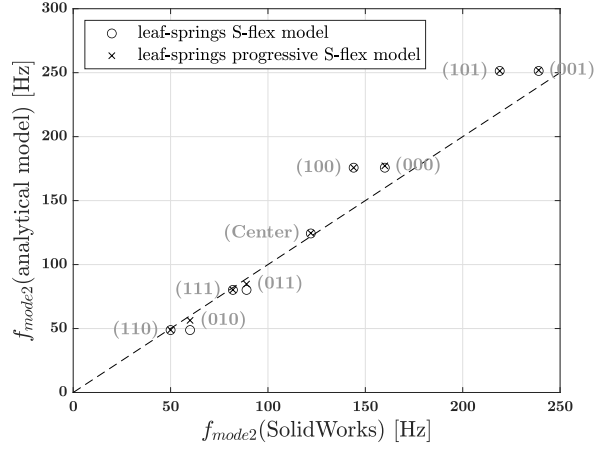


Figure 12: Comparison between the torsion mode results of the numerical approach and the analytical approach

The different stiffness can be obtained as in [20]:

- The double bending stiffness of a leaf-spring:

$$K_{Sflex,leaf} = \frac{Ewh^3}{l^3} \quad (15)$$

with its width b depending on its thickness h and its length l as described before.

- The torsion stiffness of the inertial mass:

$$K_{tors,mass} = \frac{Gw_1c_2^3}{3a_2} \quad (16)$$

with the flat mass dimensions on figure 11 and the shear modulus of glass $G = \frac{E}{2(1+\nu)}$ with $\nu = 0.17$.

- The torsion stiffness of the circular notch:

$$K_{tors,notch} = 0.284 \frac{Gbe^{2.5}}{\sqrt{r}} \quad (17)$$

with the dimensions described earlier defined according to the manufacturing process limits.

A.2.2 Results

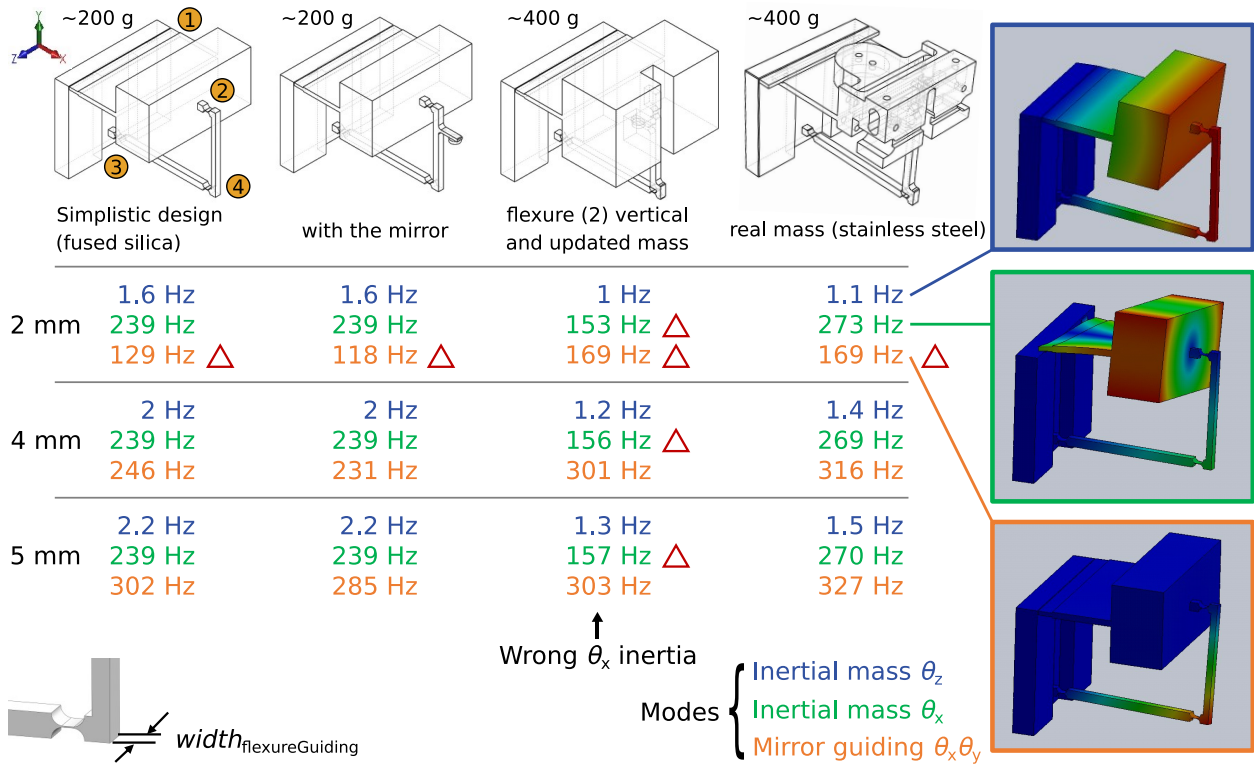


Figure 13: The design of inertial sensor mechanics is simplified to allow a quick modal analysis of a fused silica monolithic design. (1-4) represent the flexure hinge of the mechanism. The modal analysis is performed on SolidWorks. The first parameter is the width of the mirror flexure guiding. The resonance frequency of the 3 first modes is obtained. Then, the analysis is performed with different complexification of the design: first with the mirror; then, doubling the mass and changing the orientation of the hinge (2); finally, replacing the mass block with the real inertial mass design in stainless steel. The red triangles indicate that the frequency is lower than 200 Hz.

Figure 12 shows that the results of the analytical model are close to the results of the numerical approach. The label of the points correspond to the experiments listed in Table 1. The progressive S-flex model does not improve the results for all experiments. The improvement is only significant for experiments (010) and (011). Those two experiments have the widest leaf-springs. Thus, it explains why it has a greater influence. So, for the others, the deformation of the leaf-springs can be considered as constant along their width. Also, these results show that the length of the leaf-springs and their separation distance has a great influence while the thickness is less significant. Finally, taking into account the parameters of (001), a complementary study is performed on SolidWorks to verify that the spurious modes of the sensor are above 200 Hz (figure 13). Although the operating range limit is 100 Hz, a security factor is considered to avoid the non-linear effects close to the spurious modes. This experiment shows that the upper limit of the sensor's operating range is compliant with the specification (spurious modes above 100 Hz). However, using a 2 mm width mirror guiding, the spurious mode at 169 Hz may have an effect at the upper limit of the operating range.